Journal of Materials Chemistry A

ROYAL SOCIETY OF CHEMISTRY

PAPER

View Article Online
View Journal | View Issue

Open Access Article. Published on 19 May 2025. Downloaded on 6/5/2026 3:29:59 AM.
This article is licensed under a Creative Commons Attribution 3.0 Unported Licence.

Check for updates

Cite this: J. Mater. Chem. A, 2025, 13, 18842

New tetrabutylphosphonium organic ionic plastic crystals incorporating borate anions†

Haris Amir, [a] Mega Kar, [b] Luke A. O'Dell, [b] Maria Forsyth, [b] Małgorzata Swadźba-Kwaśny [a] and John D. Holbrey *[a]

Received 20th January 2025
Accepted 16th May 2025

DOI: 10.1039/d5ta00562k

rsc.li/materials-a

Organic plastic crystals have seen rapid growth in their development and potential application as solid-state electrolytes in electrochemical devices. Two tetrabutylphosphonium ($[P_{4444}]^+$) salts incorporating non-halogenated bis(butane-1,4-dioxy)borate ($[B(bdo)_2]^-$) and tetrakis(pyrazolyl)borate ($[B(pyr)_4]^-$) anions have been synthesised and their physicochemical properties characterised. Both $[P_{4444}][B(pyr)_4]$ and $[P_{4444}][B(bdo)_2]$ are solid under ambient conditions and display solid–solid thermal phase transitions suggesting the formation of plastic crystal phases, which was confirmed by observation of significant ionic conductivity and ion mobility in the solid state. $[P_{4444}][B(pyr)_4]$ showed more extensive polymorphism and greater ionic conductivity, and from the ^{31}P linewidth NMR the phosphonium cation exhibited diffusion at lower temperatures. Therefore, these are of interest as potential new halogen-free solid-state electrolyte materials.

Introduction

Organic ionic plastic crystals (OIPCs) consist of organic cations and usually symmetric anions.[1,2] OIPCs ideally incorporate desirable electrolyte properties and high ionic mobility coupled with high thermal stability, non-volatility, and non-flammability.[3] Lithium-metal cells containing OIPCs have been reported to have cycling stabilities and current density of around 0.05 and 0.5 mA cm^{-2} over more than 2000 cycles.[4] However, restricted ion transport and electrode compatibility are challenges that still remain and drive current research.[5]

The potential for structural modification in OIPCs mimics that of ionic liquids (ILs) in that both OIPCs and ILs exhibit local structural disorder, and this can, in principle, be modified or influenced by the nature of the ions incorporated into the materials. In the case of ILs, local structural disorder and poor solid-state packing of ions leads to suppression of melting points and, for OIPCs, to positional and rotational defects and disorder within a solid phase providing plasticity and enhanced diffusional vectors for ionic conductivity.[2] Indeed, OIPCs can be considered as solid state analogues of ILs[6] and salts incorporating N- and P-containing cations including ammonium,[7] pyrolidinium,[8] imidazolium,[9] and phosphonium[10–12] have been extensively studied.

The formation of an OIPC phase and its characteristics can, in principle, be modified through selective changes to the cation and anion to reduce specific cation–anion interactions, as with ILs. However, the link between ion size, shape, temperature-dependent ion dynamics, physical, and electrochemical properties is still unclear.[11,13] The formation of an OIPC is reliant on achieving a balance between a coulombic attraction that is sufficient to allow retention of a long-range crystalline lattice and minimisation in site-specific associations to allow reorientation and disordering of ions within the lattice.[11,14] It should also be noted that many IL materials can also crystallise with significant degrees of structural disorder within their unit cells (for example, see Dymon *et al.*[15]).

Incorporating boron atoms as components of electrolyte anions can provide a central site for functionalisation allowing new anion motifs to be developed,[16] and can actively contribute to advantageous SEI (solid electrolyte interphase) chemistry through formation of thin, boron-rich stable layers that increase interface stability[17,18] However, despite the desirability of borate anions as contributors towards high performance electrolytes and enhanced SEI chemistry, most work to-date on OIPCs and non-aqueous organic electrolytes in general[19] has focused on materials containing fluorinated-borate anions, including the ubiquitous tetrafluoroborate[19,20] and bis-fluoro and trifluoromethyl-sulfonylimide[21] both of which may be used with dopants that facilitate ion conduction.[22]

With the global effort to transition away from fluorine-containing electrolytes and other materials in batteries, membranes and polymeric materials due to environmental impact, sustainability, and safety of fluorinated components,

[a]The QUILL Research Centre, School of Chemistry and Chemical Engineering, Queen's University Belfast, David Keir Building, Stranmillis Road, Belfast BT9 5AG, UK. E-mail: j.holbrey@qub.ac.uk

[b]Institute for Frontier Materials, Deakin University, Geelong, Victoria 3217, Australia

† Electronic supplementary information (ESI) available: ^1H, ^{13}C, ^{11}B, and ^{31}P NMR spectra and electro-spray mass spectrometry for $Na[B(bdo)_2]$, $Na[B(pyr)_4]$, $[P_{4444}][B(bdo)_2]$ and $[P_{4444}][B(pyr)_4]$. See DOI: https://doi.org/10.1039/d5ta00562k

 This journal is © The Royal Society of Chemistry 2025

Open Access Article. Published on 19 May 2025. Downloaded on 6/5/2026 3:29:59 AM.
This article is licensed under a Creative Commons Attribution 3.0 Unported Licence.

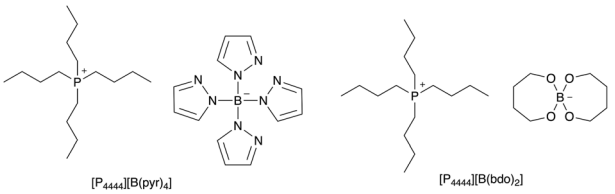

Fig. 1 Chemical structure of the two tetrabutylphosphonium salts under investigation, tetrabutylphosphonium tetrakis(pyrazolyl)borate ([P_{4444}][B(pyr)$_4$], left) and tetrabutylphosphonium bis(butane-1,4-dioxy)borate ([P_{4444}][B(bdo)$_2$], right).

new halogen-free electrolytes are increasingly sought after for both liquid and solid-state applications.[23]

A goal of our on-going work exploring the utility of fluorine-free anions in ionic liquid applications,[24] has been to explore whether new fluorine-free functional ionic materials incorporating functionalised borate anions can be developed, taking inspiration most significantly from the utility of bis(oxalato) borate ([BOB]$^-$) and related anions.[16] We describe here the synthesis and characterisation of two new tetrabutylphosphonium salts containing fluorine-free borate anions; tetrabutylphosphonium bis(butane-1,4-dioxy)borate ([P_{4444}][B(bdo)$_2$]), the 1,4-butanediol derived analogue of [P_{4444}][B(edo)$_2$], tetrabutylphosphonium bis(ethane-1,4-dioxy)borate ([P_{4444}][B(edo)$_2$]), recently described by Xu *et al.*[12] that has an *ortho*-borate anion derived from ethylene glycol/boric acid and exhibits OIPC behaviour over an uncommonly wide temperature range (−59 to 158 °C), and tetrabutylphosphonium tetrakis(pyrazolyl)borate ([P_{4444}][B(pyr)$_4$]) that incorporates an N4–coordinated borate anion (Fig. 1). The thermal properties, solid-state conductivity, and ion dynamics determined *via* ^{1}H, ^{31}P and ^{11}B solid-state wideline NMR have been investigated for these new organic ionic plastic crystals that have the potential to be used as ambient temperature solid-state electrolytes.

Experimental

Materials and methods

Acetonitrile (99.5%), acetone (99.5%), toluene (99.5%), absolute ethanol (99.5%), chloroform (99.5%), DMSO-d_6 (99.5 atom% D), $CDCl_3$ (99.8 atom% D), 1,4-butanediol (99%), sodium borohydride (98%), hexagonal boron nitride powder (98%) and boric acid (99%) were purchased from Sigma-Aldrich. Anhydrous sodium carbonate (99.5%) was purchased from Fisher Scientific, ammonium dihydrogen phosphate ($NH_4H_2PO_4$) (98%) was purchased from Alfa Aesar, 1H-pyrazole (99%) was purchased from Doug Discovery (Fluorochem), and tetrabutylphosphonium chloride (95%) was purchased from TCI. All chemicals were used as received.

Na[B(bdo)$_2$], first reported as a crystalline salt by Gainsford and Kemmitt[25] was prepared using a modification of the method described by Chiappe *et al.*[26] for sodium bis(glycerol) borate using sodium carbonate rather than NaOH, and removing co-formed water by azeotropic distillation to inhibit competing hydrolysis of labile B–O bonds in the orthoborate anion. Na[B(bdo)$_2$] is insoluble in toluene, allowing facile isolation. Na[B(pyr)$_4$] was prepared from sodium borohydride and 1*H*-pyrazole as described by Chao and Moore[27] using excess pyrazole as both solvent and to shift the substitution equilibrium to four pyrazole ligands on boron forming the tetrahedral [B(pyr)$_4$]$^-$. The two salts [P_{4444}][B(pyr)$_4$] and [P_{4444}][B(bdo)$_2$] were prepared from the corresponding sodium salts Na[B(pyr)$_4$] and Na[B(bdo)$_2$] by cation exchange with tetrabutylphosphonium chloride ([P_{4444}]Cl).

Sodium bis(butane-1,4-dioxy)borate, (Na[B(bdo)$_2$]). Boric acid (5.30 g, 80.93 mmol), butane-1,4-diol (14.5 ml, 161.73 mmol), and Na_2CO_3 (8.57 g, 80.93 mmol) were combined in toluene (100 ml). The mixture was then heated at 125 °C for 8 h., collecting evolved water in a Dean–Stark condenser. The remaining toluene was then removed *via* rotary evaporation. The crude product was dispersed in acetonitrile, stirred for 1 h. at 60 °C and collected by vacuum filtration, washed with cold ethanol (3 × 30 ml) and then dried overnight *in vacuo* at 80 °C, to give a waxy solid, yield 13.38 g, 78.7%. ^{1}H (400 MHz; DMSO-d_6; $SiMe_4$) δ 3.38 (8H, m, O–CH$_2$), 1.43 (8H, m, –CH$_2$–); ^{13}C{^{1}H} (100 MHz; DMSO-d_6; $SiMe_4$) δ 60.69 (O–CH$_2$), 29.15 (CH$_2$–CH$_2$); ^{11}B (128 MHz; DMSO-d_6; 15% $BF_3\cdot OEt_2$) δ 3.09. Calc. for $C_8H_{16}BNaO_4$: C, 51.38; H, 8.62. Found: C, 51.38; H, 8.63.

Sodium tetrakis(pyrazolyl)borate, (Na[B(pyr)$_4$]). Sodium borohydride (3.00 g, 79.30 mmol) and pyrazole (27.00 g, 400 mmol) (1 : 5 ratio) were placed into a round bottom flask under nitrogen and heated to 125 °C. The evolution of H_2 was monitored and, after 4 h., evolution of gas ceased and the reaction mixture was allowed to cool to ambient temperature. The excess pyrazole was extracted with acetone (100 ml) and the product was collected by filtration and dried overnight *in vacuo* at 80 °C, to give a white powder (yield 15.71 g, 65.6%).

^{1}H (400 MHz; DMSO-d_6; $SiMe_4$) δ 7.10 (8H, s, N–CH), 6.68 (4H, s, C–CH); ^{13}C{^{1}H} (100 MHz; DMSO-d_6; $SiMe_4$) δ 143.59 (N–CH), 125.23 (CH); ^{11}B (128 MHz; DMSO-d_6; 15% $BF_3\cdot OEt_2$) δ −6.68. Calc. for $C_{12}H_{12}BN_8Na$: C, 51.64; H, 4.33; N, 40.15. Found: C, 51.62; H, 4.35; N, 40.17.

Tetrabutylphosphonium bis(butane-1,4-dioxy)borate, ([P_{4444}][B(bdo)$_2$]). [P_{4444}]Cl (2.95 g, 10 mmol) and Na[B(bdo)$_2$] (2.73 g, 13 mmol) (1 : 1.3 ratio) were combined in $CHCl_3$ (50 ml) and stirred for 24 h under ambient conditions. Deionised water (20 ml) was then added. mixed and the organic layer was removed and washed with deionised water (5 × 20 ml) to remove traces of Na^+ and Cl^-. The solvent was removed under reduced pressure by rotary evaporation followed by drying *in vacuo* at 80 °C to give [P_{4444}][B(bdo)$_2$] as pale yellow crystals (yield 2.87 g, 64.2%). ^{1}H (400 MHz; $CDCl_3$; $SiMe_4$) δ 4.43 (8H, m, O–CH$_2$), 2.93 (8H, m, –CH$_2$–), 1.65 (8H, m, P–CH$_2$–), 0.95 (16H, m, –CH$_2$–), 0.34 (12H, t, –CH$_3$); ^{13}C{^{1}H} (100 MHz; $CDCl_3$; $SiMe_4$) δ 60.44 (O–CH$_2$), 27.86 (OCH$_2$–CH$_2$), 22.43 (d, J_{CP} = 22 Hz, P−CH$_2$), 17.39 (PCH$_2$–CH$_2$), 16.92 (–CH$_2$–), 12.10 (–CH$_3$); ^{11}B (128 MHz; $CDCl_3$; 15% $BF_3\cdot OEt_2$) δ 2.15. ^{31}P{^{1}H} (162 MHz; $CDCl_3$; 85% H_3PO_4) δ 32.99. MS (ESI) calcd for [$C_{16}H_{36}P$]$^+$ *m*/*z* 259.3; found *m*/*z* 259.2; calcd for [$C_8H_{16}BO_4$]$^-$ *m*/*z* 187.1; found *m*/*z* 187.1; Chloride content determined by XRF analysis was 219 ± 7 ppm.

Open Access Article. Published on 19 May 2025. Downloaded on 6/5/2026 3:29:59 AM. This article is licensed under a Creative Commons Attribution 3.0 Unported Licence.

Tetrabutylphosphonium tetrakis(pyrazolyl)borate, ([P_{4444}][B(pyr)$_4$]). [P_{4444}][B(pyr)$_4$] was prepared from [P_{4444}]Cl (2.95 g, 10 mmol) and Na[B(pyr)$_4$] (3.93 g, 13 mmol) (1 : 1.3 ratio) in $CHCl_3$ and produced the product as a cloudy soft solid (yield 4.15 g, 77.1%). ^{1}H (400 MHz; $CDCl_3$; Me_4Si) δ 7.51 (8H, s, –N–CH=), 7.46 (4H, s, =CH–), 1.93 (8H, m, P–CH_2–), 1.41 (16H, m, –CH_2–), 0.92 (12H, t, –CH_3); ^{13}C{^{1}H} (100 MHz; $CDCl_3$; $SiMe_4$) δ 138.46 (–N=CH–), 134.50 (–N–CH =), 103.28 (CH=CH–), 24.15 (d, J_{CP} = 12 Hz, P–CH_2), 18.95 (PCH_2–CH_2), 18.48 (–CH_2–), 13.90 (–CH_3); ^{11}B (128 MHz; $CDCl_3$; 15% $BF_3 \cdot OEt_2$) δ −6.58. ^{31}P{^{1}H} (162 MHz; $CDCl_3$; 85% H_3PO_4) δ 32.86. MS (ESI) calcd for [$C_{16}H_{36}P$]$^+$ m/z 259.3; found m/z 259.2; calcd for [$C_{12}H_{12}BN_8$]$^-$ m/z 279.1; found m/z 279.2; Chloride content determined by XRF analysis was 203 ± 9 ppm.

^{1}H, ^{13}C, ^{11}B, and ^{31}P NMR spectra and electro-spray mass spectrometry for Na[B(bdo)$_2$], Na[B(pyr)$_4$], [P_{4444}][B(bdo)$_2$] and [P_{4444}][B(pyr)$_4$] are shown in Fig. S1–16 in the ESI.†

Characterisation and analysis

NMR spectroscopy. Solution state ^{1}H, ^{13}C, ^{11}B, and ^{31}P NMR spectra for the characterisation of materials were recorded on a Bruker Avance III 400 MHz spectrometer at ambient temperature in either $CDCl_3$ or DMSO-d_6 in standard 5 mm id. borosilicate glass NMR tubes. Additional peaks observed in the ^{13}C NMR spectrum are attributed to ^{13}C–^{31}P coupling. The unassigned peak at 37 ppm in the ^{31}P spectrum is likely due to the presence of tributylphosphine oxide, a known impurity from the synthesis of the starting material [P_{4444}]Cl. Solid-state ^{11}B and ^{31}P NMR spectroscopy was performed on a Bruker Avance III 300 MHz spectrometer (operating at 96.3 MHz for ^{11}B and 121.5 MHz for ^{31}P) in 10 °C increments between −30 to 60 °C. All experiments were run and processed in TopSpin, the line widths were extracted using Dmfit.[28] Single pulse excitation was used for all experiments without any ^{1}H decoupling. Chemical shift referencing was performed using secondary references: hexagonal boron nitride powder for ^{11}B (30.4 ppm) and $NH_4H_2PO_4$ for ^{31}P (0.9 ppm).

Thermal characterisation. Thermogravimetric analysis (TGA) was performed using a Trios TGA 5500 instrument. Sample sizes ranged between 10–50 mg, platinum pans were used, and a temperature gradient of 10 °C min^{-1} from 30–1000 °C under a constant nitrogen flow of 20 ml min^{-1}. Differential scanning calorimetry (DSC) was performed using a TA Instruments Q2000 DSC. The sample size varied between 5–30 mg and sealed Tzero aluminium pans were used under a constant flow of nitrogen (50 ml min^{-1}). During DSC analysis, each sample was cooled and then heated at a rate of 10 °C min^{-1} between −90 and 150 °C (−90 and 80 °C for [P_{4444}][B(bdo)$_2$]) and cycled three times. Transition temperatures in the DSC profiles were determined using the peak maximum of the transition, and entropies of fusion were calculated from the melting endotherm area (ΔH) according to eqn (1)

$$\Delta S_{\text{fus}} = \frac{\Delta H}{T_{\text{m}}} \tag{1}$$

where T_{m} is the melting temperature in K.

Elemental analysis (CHNS) was also performed on the sodium salts using a Perkin Elemer 2400 series 2 elemental analyser. Mass spectrometry measurements were performed using a Waters LCT Premier Instrument equipped with an Advion Nanomate Infusion system. All reported mass spec data are accurate within the range of 0–10 ppm. Chloride content in the [P_{4444}]$^+$ salts was measured directly by quantitative energy dispersive X-ray fluorescence analysis (Rigaku NEX QC + QuantEZ) with analysis carried out in triplicate with an error range of ± 9 ppm.

Ionic conductivity. Electrochemical impedance spectroscopy (EIS) experiments were performed using a Biologic MTZ-35 AC impedance analyser across the frequency range from 1 Hz to 10 MHz with a peak-to-peak voltage amplitude of 0.01 V. The samples were placed in an air-tight barrel-cell fitted with Pt electrodes, designed in-house. The instrument temperature was controlled by a Eurotherm 2204e thermostat with analysis in 10 °C increments from 20 to 70 °C (with equilibrium time of 20 minutes between measurements). The conductivity of the solid electrolytes was estimated by relating the touch-down (TD) point of the Nyquist plot (see ESI†) with the following equation.

$$\sigma = \frac{1}{\text{TD}} \times \frac{\text{Thickness(cm)}}{\text{area(cm}^2)} \tag{2}$$

Results and discussion

Two new tetrabutylphosphonium borate salts containing O–O chelated [B(bdo)$_2$]$^-$ and N-coordinated [B(pyr)$_4$]$^-$ anions (Fig. 1) have been prepared from [P_{4444}]Cl by anion metathesis with the sodium salts of the respective anions. Na[B(bdo)$_2$] was first reported as a crystalline polymeric salt by Gainsford and Kemmitt[25] with the Na^+ and K^+ salts subsequently described as additives in polyether acid gas (CO_2) scrubbing applications,[29] while butyrolactone solutions of the methyltriethylammonium ([N_{1112}]$^+$) salt has been reported as a non-aqueous electrolyte formulations[30] in the patent literature.

We provide here a brief description of the thermal properties of the two [P_{4444}]$^+$ salts, highlighting the thermal characteristics to initially lead to the potential identification of OIPC behaviour. We then describe the ionic conductivities of the two salts, [P_{4444}][B(pyr)$_4$] and [P_{4444}][B(bdo)$_2$] and correlation of cation and anion dynamics determined by NMR spectroscopy, demonstrating a much more extensive region of conductivity in the solid (plastic) state than should be expected from the initial DSC thermal profile. This further suggests that, when searching for potential OIPC materials, using DSC as an initial screen may lead to many 'misses', particularly if the plastic crystal domain is large and extends to very low temperatures as was described for [P_{4444}][B(edo)$_2$],[12] the ethylene glycol-chelated analogue of [P_{4444}][B(bdo)$_2$].

Thermal properties

TGA profiles, shown in Fig. 2, indicate that both salts are thermally stable to >150 °C. In comparison, [P_{4444}][B(edo)$_2$] reported by Xu *et al.*[12] shows similar stability profile with weight loss starting around 150 °C and complete decomposition by 400 °C.

 This journal is © The Royal Society of Chemistry 2025

Open Access Article. Published on 19 May 2025. Downloaded on 6/5/2026 3:29:59 AM.
This article is licensed under a Creative Commons Attribution 3.0 Unported Licence.

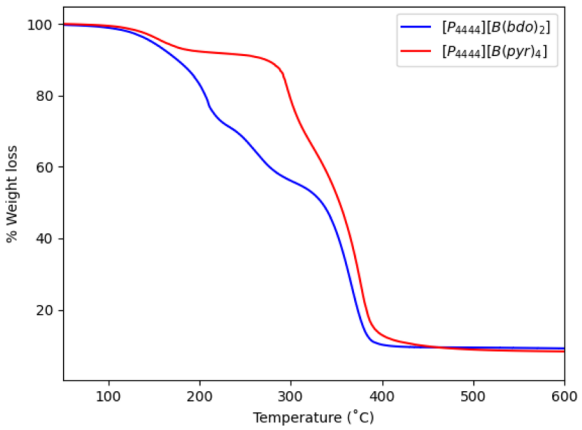

Fig. 2 TGA profiles from 50–600 °C of $[P_{4444}][B(pyr)_4]$ (red) and $[P_{4444}][B(bdo)_2]$ (blue).

DSC reveals the presence of a number of transitions in the heating and cooling cycles for both $[P_{4444}]^+$ salts, and these were repeatable across multiple thermal cycles. Data is shown from the second cycle of each sample in Fig. 3. For both salts, multiple endothermic transitions are observable, with peak positions determined from onset of each peak on heating before the solids finally melt. $[P_{4444}][B(pyr)_4]$ shows three transitions on heating as a broad, unresolved endothermic peak between *ca.* 50 °C (first onset) to 86 °C. In the cooling cycle, the reversible crystallisation and subsequent solid–solid transitions resolve into three sharp, and distinct exothermic events. $[P_{4444}][B(bdo)_2]$ melts around 60 °C with a broad, transition that appears to contain two peaks at 58 and 60 °C, and on cooling crystallises after extensive super-cooling to <10 °C with at least two distinct events evident in the DSC profile.

The entropy of fusion (ΔS_{fus}) for each phase transition was calculated using eqn (1) and is summarised in Table 1, where T_m are 69 °C and 86 °C for $[P_{4444}][B(bdo)_2]$ and $[P_{4444}][B(pyr)_4]$ respectively. The solid–solid (II–I) transition of $[P_{4444}][B(bdo)_2]$ occurs at 58 °C ($\Delta S = 5$ J K^{-1} mol^{-1}) and is followed closely by melting (I–liquid) at 60 °C ($\Delta S = 7$ J K^{-1} mol^{-1}). $[P_{4444}][B(pyr)_4]$ undergoes a first solid–solid transition (III–II) at the slightly higher temperature of 69 °C ($\Delta S = 2$ J K^{-1} mol^{-1}). The small ΔS suggests only small changes in molecular or ionic reorientation and motion occur. The second transition (II–I) at 79 °C has a more significant change in entropy associated with it ($\Delta S = 23$ J K^{-1} mol^{-1}) and is followed by melting (I–liquid) at 86 °C ($\Delta S = 5$ J K^{-1} mol^{-1}) where the change in entropy is of similar magnitude to the phase change from II–I.

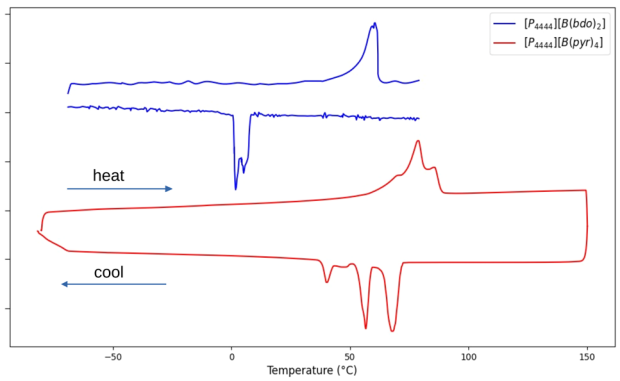

Fig. 3 DSC scan of $[P_{4444}][B(pyr)_4]$ (red) and $[P_{4444}][B(bdo)_2]$ (blue) with a scan rate of 10 °C min^{-1} (endothermic up).

Table 1 DSC transitions on heating

Sample	Transition	Peak (onset)/°C	ΔS_{fus}/J K^{-1} mol^{-1}
$[P_{4444}][B(bdo)_2]$	II–I	58 (48)	5
	I–liquid	61 (60)	7
$[P_{4444}][B(pyr)_4]$	III–II	69 (66)	2
	II–I	79 (74)	23
	I–liquid	86 (83)	5

The transition shown for $[P_{4444}][B(pyr)_4]$ in Fig. 3 (and listed in Table 1) are all broad and poorly resolved merging over the range 58–86 °C, however, on cooling, these resolve into two distinct, well separated events at 68 °C and 57 °C, followed by broader and less exothermic transitions at 47 °C and finally at 40 °C.

For both salts, the DSC melting profiles show a long broad onset to melting which is characteristic of a gain in rotational or translational disorder prior to melting of the lattice and is consistent with plastic behaviour, as is the observation of multiple phase transitions. The melting entropy (ΔS_{melt}) for $[P_{4444}][B(bdo)_2]$ (7 J K^{-1} mol^{-1}) and $[P_{4444}][B(pyr)_4]$ (5 J K^{-1} mol^{-1}) are significantly lower than Timmermans' threshold (<20 J K^{-1} mol^{-1})[31] thereby classifying these materials as plastic crystals.

Compared to $[P_{4444}][B(edo)_2]$ (mp 158 °C), the mps of $[P_{4444}][B(pyr)_4]$ (86 °C) and $[P_{4444}][B(bdo)_2]$ (60 °C) are significantly reduced. In addition, on further cooling in the DSC, no further low temperature thermal events were observed. This contrasts to $[P_{4444}][B(edo)_2]$ where an exceptionally low temperature first-order solid–solid transition at −59 °C was reported giving an OIPC phase range of almost 240 °C between *ca.* −59–158 °C.

However, it is important to note that multiple phase transitions alone are not definitive indicators of OIPC formation. While these transitions suggest the potential for orientational flexibility – a hallmark of OIPC behaviour – they are not the sole markers of plastic crystal characteristics. Additional factors, such as the material's ability to retain a pseudo-crystalline state across transitions and structural disorder at the molecular level are also critical in establishing a true OIPC.

Conductivity

The conductivities of $[P_{4444}][B(pyr)_4]$ and $[P_{4444}][B(bdo)_2]$ were determined by EIS between 20–70 °C in order to scan across the phase transitions observed by DSC. The samples were not heated above their respective melting points due to the barrel-cell not being designed for liquid samples. The solid state conductivity of $[P_{4444}][B(pyr)_4]$ and $[P_{4444}][B(bdo)_2]$ as a function of temperature is shown in Table 2 and in Fig. 4 as an Arrhenius plot (eqn (3)).

Open Access Article. Published on 19 May 2025. Downloaded on 6/5/2026 3:29:59 AM.
This article is licensed under a Creative Commons Attribution 3.0 Unported Licence.

Table 2 Conductivity σ (S cm^{-1}), activation energy E_a (kJ mol^{-1}) and the quality of fit (R^2) to eqn (3) for [P_{4444}][B(pyr)$_4$] and [P_{4444}][B(bdo)$_2$] over the temperature range 20–70 °C

	σ/S cm^{-1}	
Temperature/K	[P_{4444}][B(bdo)$_2$]	[P_{4444}][B(pyr)$_4$]
293	1.55×10^{-7}	8.85×10^{-7}
303	5.20×10^{-7}	1.57×10^{-6}
313	9.13×10^{-7}	3.07×10^{-6}
323	1.87×10^{-6}	4.57×10^{-6}
333	—	6.87×10^{-6}
343	—	8.89×10^{-6}
E_a	51.9[a]	32.2[b], 47.4[c]
R^2	>0.9996	>0.996

[a] Between 303–323 K. [b] Between 313–343 K. [c] Between 293–313 K.

$$\ln \sigma = -\frac{E_a}{RT} + A \quad (3)$$

where σ is conductivity, E_a is the activation energy, R is the molar gas constant and A is a coefficient constant. E_a can be determined from the slope of the line.

The temperature-dependent conductivity measurements (Fig. 4) show that both salts are conductive at temperatures below the respective endothermic transitions observed by DSC (Table 1) at 50–86 °C for [P_{4444}][B(pyr)$_4$] and 50–60 °C for [P_{4444}][B(bdo)$_2$]. This suggests a high degree of disorder or defects enabling conductivity in the solid state at, and below, ambient temperature. Plastic crystal formation is supported by the ion mobilities determined from wide-line NMR spectroscopy described below and, with the absence of a large ($\Delta S \gg 20$ J K^{-1} mol^{-1}) solid–solid transition below the II-I transition for [P_{4444}][B(bdo)$_2$] and below the III–II transition for [P_{4444}][B(pyr)$_4$] allows the tentative conclusion that these materials are also plastic crystals at lower temperatures with a possible plastic → ordered crystal transition below the lower limit of scanning on the DSC, *e.g.* below −75 °C.

It is important to note that while the wideline NMR data were collected down to 243 K (−30 °C), the conductivity measurements were limited to 293 K (20 °C). This temperature range was chosen to focus on the practical operating conditions relevant to solid-state electrolyte applications. However, extending conductivity measurements to lower temperatures in future studies would provide further insight into the ionic transport mechanisms across a broader temperature range.

[P_{4444}][B(pyr)$_4$] showed higher conductivity than [P_{4444}][B(bdo)$_2$] and, for both salts, the conductivities increase by an order of magnitude from 8.85×10^{-7} S cm^{-1} to 8.89×10^{-6} S cm^{-1} for [P_{4444}][B(pyr)$_4$] between 293–343 K, and from 1.55×10^{-7} S cm^{-1} to 1.87×10^{-6} S cm^{-1} between 293–323 K for [P_{4444}][B(bdo)$_2$].

It is notable that the conductivities of both [P_{4444}][B(pyr)$_4$] and [P_{4444}][B(bdo)$_2$] in the solid state are comparable to the reported values for other tetraalkylphosphonium-based OIPCs.[10,12] For example, the conductivity of [P_{4444}][B(bdo)$_2$] at 293 K (1.55×10^{-7} S cm^{-1}) is the same as that reported by Xu *et al.*[12] for tetrabutylammonium bis(ethylene-dioxyl)borate. At 293 K, [P_{4444}][bis(glycolato)borate] was reported to have a higher conductivity of 2.3×10^{-6} S cm^{-1}, however for the corresponding tetrabutylammonium analogue, [N_{4444}][bis(glycolato)borate], conductivity is reduced to 1.0×10^{-7} S cm^{-1}. It is worth noting that [P_{4444}][BOB], an IL at 293 K is 2.8×10^{-5} S cm^{-1}. Compared to OIPCs containing smaller asymmetric tetraalkylphosphonium cations,[10] [P_{4444}][B(pyr)$_4$] displayed greater conductivity than [P_{1444}][BF_4] and [P_{1224}][BF_4], while the less conductive [P_{4444}][B(bdo)$_2$] was intermediate between [P_{1224}][BF_4] and [P_{1444}][BF_4].

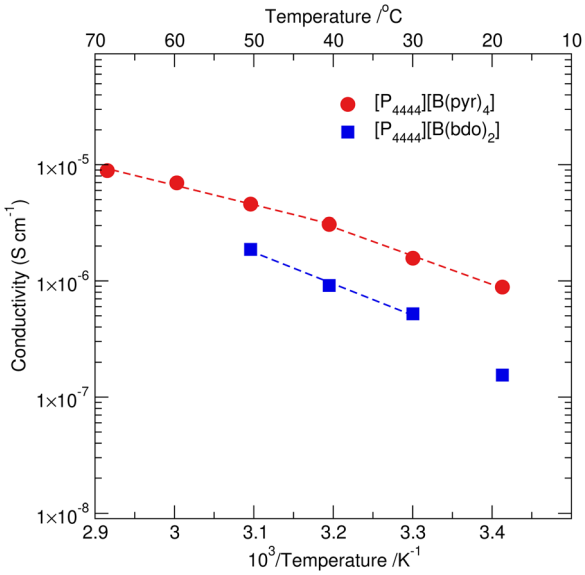

Fig. 4 Arrhenius plot of the conductivity of [P_{4444}][B(pyr)$_4$] (red) and [P_{4444}][B(bdo)$_2$] (blue). Dashed lines represent fits to the Arrhenius equation with activation energy, E_a, of 51.9 kJ mol^{-1} for [P_{4444}][B(bdo)$_2$] between 303–323 K, 32.2 kJ mol^{-1} for [P_{4444}][B(pyr)$_4$] between 312–343 K and 47.4 kJ mol^{-1} for [P_{4444}][B(pyr)$_4$] between 293–313 K (all with $r^2 > 0.996$).

From the Arrhenius plot of log(conductivity) *vs.* reciprocal temperature shown in Fig. 4, both [P_{4444}][B(bdo)$_2$] and [P_{4444}][B(pyr)$_4$] show similar changes in conductivity with temperature. A small change in slope appears for [P_{4444}][B(pyr)$_4$] at 313 K which may be due to a change in the dominant ion transport mechanism or subtle phase behaviour changes within the plastic crystal domain. Fitting to the Arrhenius equation between 313–343 and 293–313 K, activation energies (E_a) of 32.2 and 47.4 kJ mol^{-1} respectively, with $r^2 > 0.996$. For [P_{4444}][B(bdo)$_2$], a drop in conductivity can be seen at the lowest temperature measured (293 K, $\sigma = 1.55 \times 10^{-7}$ S cm^{-1}) and E_a, determined between 303–323 K, was 51.9 kJ mol^{-1}. The lower E_a of [P_{4444}][B(pyrazole)$_4$] compared to [P_{4444}][B(bdo)$_2$] is likely due to the larger, more bulky borate anion that will show a greater sensitivity to temperature change in comparison to the smaller [B(bdo)$_2$]$^-$.

Despite the absolute conductivity values of [P_{4444}][B(bdo)$_2$] and [P_{4444}][B(pyr)$_4$] (1.55×10^{-7}–8.89×10^{-6} S cm^{-1} between 293–343 K) being greater than some analogues, they remain less conductive than fluorinated OIPCs (*e.g.*, [P_{1444}][FSA] > 1.70 ×

Open Access Article. Published on 19 May 2025. Downloaded on 6/5/2026 3:29:59 AM.
This article is licensed under a Creative Commons Attribution 3.0 Unported Licence.

10^{-3} S cm^{-1} at 313 K).[10] This limitation reflects the trade-off between eliminating fluorine (for safety and sustainability) and achieving the highest ionic transport rates. Future work will focus on molecular and structural modifications to bridge this gap.

Wideline solid state nuclear magnetic resonance (NMR) spectroscopy

Cation and anion dynamics were investigated over the temperature range 243–343 K using static (wideline) ^{31}P and ^{11}B NMR spectroscopy, with spectral analysis modelled using Dmfit.[28] For ^{31}P spectra, with spin $I = \frac{1}{2}$, the chemical shift anisotropy (CSA) model was applied. Whereas for ^{11}B nuclei where quadrupolar interactions have a more significant influence on signals and the CSA model is less effective, dynamics were assessed by examining the full width at half maximum (FWHM) and linewidths of ^{11}B signals.

Wideline ^{31}P and ^{11}B NMR signals from [P_{4444}][B(bdo)$_2$] and [P_{4444}][B(pyr)$_4$] over the temperature range 243–343 K are shown in Fig. 5. At 243 K, the ^{31}P NMR signal from [P_{4444}][B(bdo)$_2$] presents as a broad band (line width >5000 Hz) with a secondary sharp component, with both signals centred at the same chemical shift suggesting that this reflects dynamics rather than formation of different chemical species and is characteristic of a material containing a bulk of static components (the broad signal) and a small concentration of mobile species. On increasing temperature, from 243–343 K, the broad peak reduces in intensity and the sharp signal (line width <1000 Hz), representing mobile dynamic cations, becomes dominant from 303 K. For [P_{4444}][B(pyr)$_4$], the ^{31}P signal is far less broad at 243 K with a line width of *ca.* 2000 Hz that sharpens with increasing temperature to <1000 Hz by 283–293 K mapping to the line width seen for [P_{4444}][B(bdo)$_2$].

The ^{31}P signals for [P_{4444}][B(bdo)$_2$] and [P_{4444}][B(pyr)$_4$] were deconvoluted into the broad and sharp peak components using dmfit. The contributions of the two components from [P_{4444}][B(bdo)$_2$] at 253 K are shown in Fig. 6 and the line width of the dominant species (static or mobile) is plotted as a function of temperature in Fig. 7.

For the [P_{4444}]$^+$ cation in both [P_{4444}][B(bdo)$_2$] and [P_{4444}][B(pyr)$_4$], a reduction in line width of the broad component as the temperature is raised from 243–293 K can be clearly seen, and from around 303 K, both solid salts contain dynamic [P_{4444}]$^+$ cations characterised by the sharp ^{31}P NMR signal (line width <1000 Hz). The ^{31}P NMR signal for [P_{4444}][B(bdo)$_2$] shows a large reduction in line width between 243–293 K, with a transformation of the NMR signal from static to almost wholly dynamic character. For [P_{4444}][B(pyr)$_4$], the change in line width is smaller, due to the presence of a larger dynamic component in the salt even at 243 K. It is notable that this increase in the cation dynamics and the switch to a single, sharp signal above 303 K for both salts does not appear to be associated with any of the thermal events observed from DSC (Fig. 3), but is consistent with the conductivity measured even below the transition temperatures.

Dynamics of the [B(bdo)$_2$]$^-$ and [B(pyr)$_4$]$^-$ anions were examined using the corresponding ^{11}B NMR data shown in Fig. 5. Compared to the cation ^{31}P NMR signals, there is less evidence for large changes in the ^{11}B signals with temperature. For both [P_{4444}][B(bdo)$_2$] and [P_{4444}][B(pyr)$_4$], the ^{11}B NMR presents a broad signal (*ca.* 500–1000 Hz) with a shoulder at higher frequency. For [P_{4444}][B(pyr)$_4$], the ^{11}B NMR signal also contains some unresolved additional structure within the major

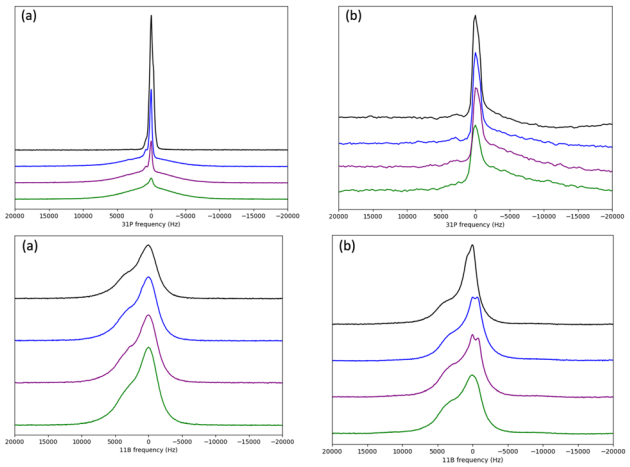

Fig. 5 Stacked wide line static solid state ^{31}P (top) and ^{11}B (bottom) NMR signals from at various temperatures [P_{4444}][B(bdo)$_2$] (a, left) and [P_{4444}][B(pyr)$_4$] (b, right) at T = 243 K (green), 273 K (purple), 303 K (blue), and 343 K (black).

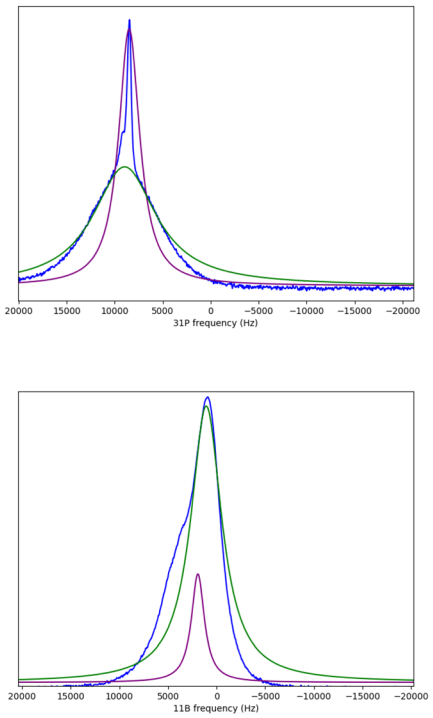

Fig. 6 Solid state, wideline ^{31}P (top) and ^{11}B (bottom) NMR spectrum of [P_{4444}][B(bdo)$_2$] at 253 K (−20 °C) showing deconvolution into the broad (static) contribution in green and sharper (mobile) contributions in purple.

Open Access Article. Published on 19 May 2025. Downloaded on 6/5/2026 3:29:59 AM.
This article is licensed under a Creative Commons Attribution 3.0 Unported Licence.

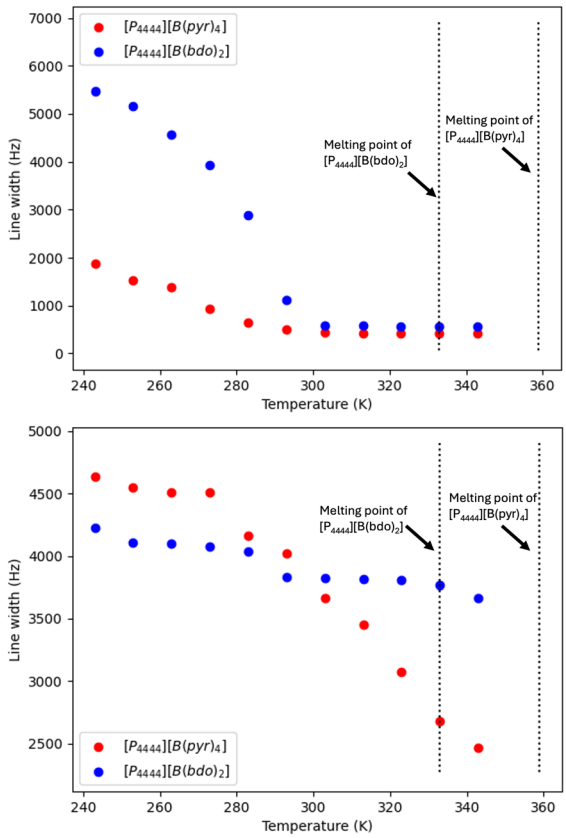

Fig. 7 Line width (Hz) of ^{31}P (top) and ^{11}B (bottom) static NMR signals from $[P_{4444}][B(bdo)_2]$ and $[P_{4444}][B(pyr)_4]$ over the temperature range 243–343 K.

signals. The asymmetric shape of the signal may be due to the sensitivity of the quadrupolar ^{11}B to magnetic anisotropy from the solid state environment and from the quadrupolar N-atoms coordinating to the B-centre.

Deconvolution of the dominant symmetric signal within the composite ^{11}B signal using dmfit allows separation of the broad and sharper peak components. These are shown independently in Fig. 6. The broader peak, corresponding to static solid boron nuclei, is the most dominant component at this temperature (253 K), this is repeated at each temperature between 243–343 K for ^{11}B for $[P_{4444}][B(bdo)_2]$ and $[P_{4444}][B(pyr)_4]$ as shown in Fig. 5. The line width of the more dominant species (static or mobile) is plotted against temperature, as shown in Fig. 7.

The line width of the ^{11}B signals in both OIPCs (Fig. 5) show very little change. The signal for $[P_{4444}][B(pyr)_4]$ has a line width at half height of *ca.* 4500 Hz and is retained between 243–273 K before becoming sharper and narrower between 273–343 K with a monotonic reduction in line width of *ca.* 50% to 2500 Hz, which is of the same order as that reported from solid state studies of a range of boronate esters[32] and it is unlikely that the borate anion is mobile so any mobile component from the interpretation of the conductivity results above could reflect rotation[11] that would yield a more isotropic magnetic environment. For $[P_{4444}][B(bdo)_2]$, the ^{11}B NMR signal shows little variation with temperature, with the linewidth decreasing from *ca.* 4250–3750 Hz between 243–343 K. Again, this suggests that the borate anions are not dynamic and so are not the predominant charge carriers for the two OIPCs.

Conclusion

This work has introduced two new fluorine-free borate anion motifs through the synthesis of $Na[B(pyr)_4]$ and $Na[B(dbo)_2]$ and subsequent transformation to tetrabutylphosphonium salts $[P_{4444}][B(pyr)_4]$ and $[P_{4444}][B(bdo)_2]$. The thermal behaviour of the $[P_{4444}]^+$ salts was studied using DSC, and an initial identification of potential organic ionic plastic crystal (OIPC) phases in both salts was made based on observation of multiple low-energy, reversible solid–solid transitions were observed between 50–90 °C. Conductivity measurements further supported this observation, revealing unexpectedly high ionic conductivities (1.57×10^{-6} S cm^{-1} for $[P_{4444}][B(pyr)_4]$ and 5.20×10^{-7} S cm^{-1} at 303 K) comparable to other phosphonium-based OIPCs, even below the observed phase transition temperatures. These findings suggest a high degree of disorder in the room-temperature phase, confirmed by wideline solid-state NMR and linewidth analysis, which showed increased cation mobility between 240–293 K and indicate the potential to incorporate these and related[12] new fluorine-free O–O chelated and N-coordinated borate anions into the development of advanced ionic electrolytes both as OIPCs and potentially as ILs.

Data availability

The data supporting this article have been included as part of the ESI.†

Conflicts of interest

There are no conflicts to declare.

Acknowledgements

The authors thank the Australian Research Council for support and funding through the IC180100049 (storEnergy).

Notes and references

1 (*a*) M. L. Thomas, K. Hatakeyama-Sato, S. Nanbu and M. Yoshizawa-Fujita, *Energy Adv.*, 2023, **2**, 748–764; (*b*) L. Jin, P. C. Howlett, J. M. Pringle, J. Janikowski, M. Armand, D. R. MacFarlane and M. Forsyth, *Energy Environ. Sci.*, 2014, **7**, 3352–3361; (*c*) Y. Abu-Lebdeh, P. Alarco, A. Abouimrane, L. Ionescu-Vasii, A. Hammami, M. Armand and J. New Mat, *Electr. Sys.*, 2005, **8**, 197; (*d*) Y. Abu-Lebdeh, A. Abouimrane, P.-J. Alarco and M. Armand, *J. Power Sources*, 2006, **154**, 255–261; (*e*) Y. Abu-Lebdeh, A. Abouimrane, P.-J. Alarco, I. Dividson and M. Armand, *J. Power Sources*, 2006, **159**, 891–893; (*f*) T. Rüther, J. Huang and A. F. Hollenkamp, *Chem. Commun.*, 2007, 5226–5228; (*g*) Z.-B. Zhou and H. Matsumoto, *Electrochem. Commun.*, 2007, **9**, 1017–1022;

 This journal is © The Royal Society of Chemistry 2025

Open Access Article. Published on 19 May 2025. Downloaded on 6/5/2026 3:29:59 AM. This article is licensed under a Creative Commons Attribution 3.0 Unported Licence.

(*h*) Y. Abu-Lebdeh, E. Austin and I. J. Davidson, *Chem. Lett.*, 2009, **38**, 782–783.

2 F. Makhlooghiazad, R. Yunis, D. Mecerreyes, M. Armand, P. C. Howlett and M. Forsyth, *Solid State Ionics*, 2017, **312**, 44–52.

3 P. C. Howlett, J. Sunarso, Y. Shekibi, E. Wasser, L. Jin, D. R. MacFarlane and M. Forsyth, *Solid State Ionics*, 2011, **204**, 73–79.

4 (*a*) P. C. Howlett, Y. Shekibi, D. R. MacFarlane and M. Forsyth, *Adv. Eng. Mater.*, 2009, **11**, 1044–1048; (*b*) A. Lennert, K. Wagner, R. Yunis, J. M. Pringle, D. M. Guldi and D. L. Officer, *ACS Appl. Mater. Interfaces*, 2018, **10**, 32271–32280.

5 H. Zhu, D. R. MacFarlane, J. M. Pringle and M. Forsyth, *Trends Chem.*, 2019, **1**, 126–140.

6 D. R. MacFarlane, M. Forsyth, P. C. Howlett, M. Kar, S. Passerini, J. M. Pringle, H. Ohno, M. Watanabe, F. Yan, W. Zheng, *et al.*, *Nat. Rev. Mater.*, 2016, **1**, 1–15.

7 (*a*) C. Shi, S. Li, W. Zhang, L. Qiu and F. Yan, *J. Mater. Chem. A*, 2013, **1**, 13956–13962; (*b*) W. A. Henderson, D. M. Seo, Q. Zhou, P. D. Boyle, J.-H. Shin, H. C. De Long, P. C. Trulove and S. Passerini, *Adv. Energy Mater.*, 2012, **2**, 1343–1350.

8 D. R. MacFarlane, J. Huang and M. Forsyth, *Nature*, 1999, **402**, 792–794.

9 M. Lee, Y.-H. Lee, J. H. Park and U. H. Choi, *Org. Electron.*, 2017, **48**, 241–247.

10 V. Armel, D. Velayutham, J. Sun, P. C. Howlett, M. Forsyth, D. R. MacFarlane and J. M. Pringle, *J. Mater. Chem.*, 2011, **21**, 7640–7650.

11 L. Jin, K. M. Nairn, C. M. Forsyth, A. J. Seeber, D. R. MacFarlane, P. C. Howlett, M. Forsyth and J. M. Pringle, *J. Am. Chem. Soc.*, 2012, **134**, 9688–9697.

12 Y. Xu, A. Reinholdt, O. N. Antzutkin, M. Forsyth, P. Johansson and F. U. Shah, *Cryst. Growth Des.*, 2024, **24**, 8989–8998.

13 J. Adebahr, F. C. Grozema, S. W. Deleeuw, D. R. MacFarlane and M. Forsyth, *Solid State Ionics*, 2006, **177**, 2845–2850.

14 (*a*) D. R. MacFarlane and M. Forsyth, *Adv. Mater.*, 2001, **13**, 957–966; (*b*) H. Zhu, F. Chen, L. Jin, L. A. O'Dell and M. Forsyth, *ChemPhysChem*, 2014, **15**, 3720–3724.

15 J. Dymon, R. Wibby, J. Kleingardner, J. M. Tanski, I. A. Guzei, J. D. Holbrey and A. S. Larsen, *Dalton Trans.*, 2008, 2999–3006.

16 (*a*) W. Xu and C. A. Angell, *Electrochem. Solid-State Lett.*, 2001, **4**, L3; (*b*) K. Xu, S. Zhang, T. R. Jow, W. Xu and C. A. Angell, *Electrochem. Solid-State Lett.*, 2001, **5**, A26.

17 (*a*) Z. Liu, A. Patra and N. Matsumi, *ACS Appl. Energy Mater.*, 2025, **8**, 3360–3368; (*b*) J. Li, Y. Long, L. Li, F. Pu, W. Liao, X. Yu, H. Liao and X. Hu, *New J. Chem.*, 2025, **49**, 1755–1762; (*c*) N. R. Park, M. Zhang, B. Han, W. Li, K. Qian, H. Nguyen, S. Kumakura and Y. S. Meng, *Adv. Energy Mater.*, 2024, **14**, 2401968.

18 (*a*) D. Zhu, J. Xu, K. Ding, Q. Xu, P. Shi and Y. Min, *Adv. Funct. Mater.*, 2023, **33**, 2213822; (*b*) L. Ma, J. Tan, Y. Wang, Z. Liu, Y. Yang, T. Gray, X. Zhang, M. Ye and J. Shen, *Adv. Energy Mater.*, 2023, **13**, 2300042; (*c*) C. Bodin, J. Forero Saboya, P. Jankowski, K. Radan, D. Foix, C. Courrèges, I. Yousef, R. Dedryvère, C. Davoisne, M. Lozinšek and A. Ponrouch, *Batteries Supercaps*, 2022, **6**, e202200433; (*d*) J. Sheng, Q. Zhang, M. Liu, Z. Han, C. Li, C. Sun, B. Chen, X. Zhong, L. Qiu and G. Zhou, *Nano Lett.*, 2021, **21**, 8447–8454; (*e*) Q. Xie, W. Li, A. Dolocan and A. Manthiram, *Chem. Mater.*, 2019, **31**, 8886–8897.

19 (*a*) K. Xu, *Chem. Rev.*, 2004, **104**, 4303–4418; (*b*) K. Xu, *Chem. Rev.*, 2014, **114**, 11503–11618.

20 (*a*) C. S. M. Kang, O. E. Hutt and J. M. Pringle, *ChemPhysChem*, 2022, **23**, e202200115; (*b*) F. Nti, L. Porcarelli, G. W. Greene, H. Zhu, F. Makhlooghiazad, D. Mecerreyes, P. C. Howlett, M. Forsyth and X. Wang, *J. Mater. Chem. A*, 2020, **8**, 5350–5362; (*c*) R. Yunis, J. M. Pringle, X. Wang, G. M. A. Girard, R. Kerr, H. Zhu, P. C. Howlett, D. R. MacFarlane and M. Forsyth, *J. Mater. Chem. A*, 2020, **8**, 14721–14735; (*d*) N. Iranipour, D. J. Gunzelmann, A. J. Seeber, J. Vongsvivut, A. F. Hollenkamp, M. Forsyth and P. C. Howlett, *J. Mater. Chem. A*, 2017, **5**, 24909–24919; (*e*) T. J. Stockmann and Z. Ding, *J. Phys. Chem. B*, 2012, **116**, 12826–12834.

21 (*a*) J. Sun, C. S. M. Kang, G. Huang, F. M. F. Vallana, A. Kumar, L. A. O'Dell, M. Galceran, O. Hutt, P. C. Howlett, M. Forsyth and J. M. Pringle, *J. Mater. Chem. A*, 2023, **11**, 22329–22339; (*b*) Y. Garcia, L. Porcarelli, H. Zhu, D. Mecerreyes, M. Forsyth and L. A. O'Dell, *J. Mater. Chem. A*, 2024, **12**, 4146–4158.

22 (*a*) J. Luo, O. Conrad and I. F. J. Vankelecom, *J. Mater. Chem. A*, 2013, **1**, 2238–2247; (*b*) M. Forsyth, T. Chimdi, A. Seeber, D. Gunzelmann and P. C. Howlett, *J. Mater. Chem. A*, 2014, **2**, 3993–4003; (*c*) X. Chen, H. Tang, T. Putzeys, J. Sniekers, M. Wubbenhorst, K. Binnemans, J. Fransaer, D. E. De Vos, Q. Li and J. Luo, *J. Mater. Chem. A*, 2016, **4**, 12241–12252; (*d*) X. Li, Z. Zhang, S. Li, K. Yang and L. Yang, *J. Mater. Chem. A*, 2017, **5**, 21362–21369.

23 (*a*) Y. Xu, A. Filippov, S. Bhowmick, P. Johansson and F. U. Shah, *Energy Adv.*, 2024, **3**, 564–573; (*b*) G. Hernández, R. Mogensen, R. Younesi and J. Mindemark, *Batteries Supercaps*, 2022, **5**, e202100373; (*c*) R. Mogensen, A. Buckel, S. Colbin and R. Younesi, *Chem. Mater.*, 2021, **33**, 1130–1139; (*d*) L. O. S. Colbin, R. Mogensen, A. Buckel, Y. Wang, A. J. Naylor, J. Kullgren and R. Younesi, *Adv. Mater. Interfaces*, 2021, **8**, 2101135.

24 (*a*) A. McGrogan, E. L. Byrne, R. Guiney, T. F. Headen, T. G. A. Youngs, A. Chrobok, J. D. Holbrey and M. Swadźba-Kwaśny, *Phys. Chem. Chem. Phys.*, 2023, **25**, 9785–9795; (*b*) L. Wang, G. A. Nelson, J. Toland and J. D. Holbrey, *ACS Sustainable Chem. Eng.*, 2020, **8**, 13362–13368; (*c*) L. Moura, L. C. Brown, M. Blesic and J. D. Holbrey, *ChemPhysChem*, 2017, **18**, 3384–3389.

25 G. J. Gainsford and T. Kemmitt, *Acta Crystallogr., Sect. C*, 2005, **61**, m136–m138.

26 C. Chiappe, F. Signori, G. Valentini, L. Marchetti, C. S. Pomelli and F. Bellina, *J. Phys. Chem. B*, 2010, **114**, 5082–5088.

Open Access Article. Published on 19 May 2025. Downloaded on 6/5/2026 3:29:59 AM.
This article is licensed under a Creative Commons Attribution 3.0 Unported Licence.

27 S. Chao and C. E. Moore, *Anal. Chim. Acta*, 1978, **100**, 457–467.
28 D. Massiot, F. Fayon, M. Capron, I. King, S. Le Calvé, B. Alonso, J. Durand, B. Bujoli, Z. Gan and G. Hoatson, *Magn. Reson. Chem.*, 2001, **40**, 70–76.
29 C. R. Laroche, Composition comprising organoborates and physical solvents and use thereof for the removal of acid gases from hydrocarbon fluid streams, WO Pat. App. WO2017180285, 2017.
30 Y. Washio, N. Takeishi, H. Shimamoto, K. Mori, N. Ushio, K. Shiono, T. Kishi and H. Samura, An electrolyte for use in electrolytic capacitors, *Eur. Pat.*, App. EP381936, 1990.
31 J. Timmermans, *J. Phys. Chem. Solids*, 1961, **18**, 1–8.
32 J. W. Weiss and D. L. Bryce, *J. Phys. Chem. A*, 2010, **114**, 5119–5131.

 This journal is © The Royal Society of Chemistry 2025